LARGE EDDY SIMULATION OF THE FLOW AROUND AN AEROSPATIALE A-AEROFOIL

S. Dahlström[*], L. Davidson[†]

Department of Thermo and Fluid Dynamics
Chalmers University of Technology
SE-412 96 Göteborg, Sweden
[*] e-mail: sd@tfd.chalmers.se, webpage: http://www.tfd.chalmers.se/~sd/project.html
[†] e-mail: lada@tfd.chalmers.se, webpage: http://www.tfd.chalmers.se/~lada

Key words: Large Eddy Simulation, Finite Volume, Airfoil, Transition, Approximate Wall Boundary Condition, Upwinding.

Abstract. *The work presented in this paper is part of the ongoing Brite-Euram project LESFOIL. In the project, Large Eddy Simulation (LES) is used to calculate the flow around the Aerospatiale A-profile at an angle of attack of 13.3° and a chord Reynolds number of $2.1 \cdot 10^6$.*

The method used is an incompressible implicit second-order finite volume method with a collocated grid arrangement. To suppress unphysical oscillations (mainly generated from the leading edge area), upwinding is used in front of the airfoil and upstream of the transition point. In the transition region, the scheme is gradually mixed with the central difference scheme (CDS). The non-dissipative CDS gives rise to numerical oscillations and the boundary layer is tripped numerically. Although the transition is unnatural, the unphysical oscillations are dampened in the area downstream of the transition.

Four simulations have been carried out, one using an approximate wall boundary condition and the other three using the no-slip condition. None of the present computations predict separation. However, the importance of the spanwise resolution is demonstrated in these attached boundary layer simulations. Before any conclusions are drawn about the feasibility of LES for this case, the number of nodes in the wall-normal direction must be increased or some other approach has to be applied in order to treat the coarse resolution in the laminar boundary layer.

1

1 INTRODUCTION

The feasibility of Large Eddy Simulations (LES) of flows around simple, 2D airfoils is investigated in the LESFOIL project (see [1], where the project is presented). The airfoil case chosen is the flow around the Aerospatiale A-airfoil at an angle of attack, α, of 13.3°. The chord Reynolds number is $2.1 \cdot 10^6$ and the flow is subsonic with a freestream Mach number of 0.15. These are high-lift conditions at take-off and landing. The flow around the Aerospatiale A-airfoil has been the subject of extensive study. Different CFD codes (steady and unsteady RANS, compressible and incompressible methods) were validated in the EUROVAL project [2] and in the ECARP project [3] on this particular single-element airfoil. It was found that few RANS models are capable of handling this flow problem, mainly because of the lack of curvature effects in the eddy-viscosity models. The second-moment closures (which do take into account curvature effects) produced the best results, see also Refs. [4–6]. Much because of the rate at which computer power is increasing, LES is becoming an interesting approach applicable for more complex flows.

This is a challenging case for LES owing to the high Reynolds number and because of the different flow regimes around the airfoil, which are sketched in Fig. 1. At the leading edge there is a very thin laminar boundary layer. On the pressure side, this boundary layer is tripped at 30% of the chord and there is a transition to a very thin turbulent boundary layer. On the suction side, there is a peak in the pressure near the leading edge. The favorable pressure gradient accelerates the flow around the leading edge. In this case the flow separates, a separation bubble is formed and, when the flow reattaches at about 12% of the chord, the boundary layer becomes turbulent. The boundary layer grows under the influence of an adverse pressure gradient and, at about 82.5% of the chord, the flow separates. In the wake, downstream of the trailing edge, the low-speed flow from the separation region on the suction side forms a mixed shear layer with the flow from the very thin boundary layer on the pressure side.

Even at the from an aeronautical point of view low Reynolds number, a wall-resolved LES is too expensive. The use of approximate boundary conditions in the near-wall region is necessary and a good method of prescribing and controlling the transition is
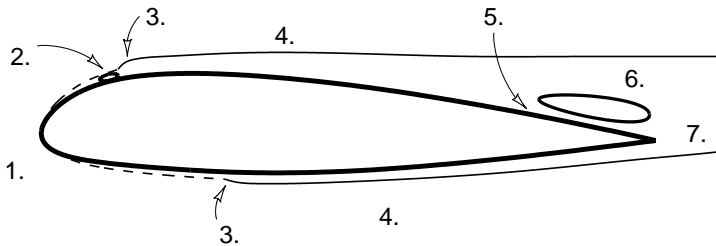

Figure 1: Schematic sketch of the flow regimes around the Aerospatiale A-profile: 1. laminar boundary layer, 2. laminar separation bubble, 3. transition region, 4. turbulent boundary layer, 5. separation point, 6. separation region, 7. wake region.

needed. Still, the requirements on the mesh are demanding and result in meshes with a large number of nodes. For this reason, an efficient numerical method with an effective parallelization is needed.

Results from four computations on two meshes are presented, with focus on the last three, where upwinding is used in part of the domain to prescribe the transition and suppress unphysical oscillations. The outline of this paper is: the following two sections summarize the numerical method and boundary conditions. The upwinding/central difference scheme is presented in section 4 and then the two meshes and an approximate boundary condition are described in section 5 and 6, respectively. The convergence criteria are discussed and speed-up results are presented in section 7. In section 8 the results are presented and in the last section conclusions are drawn.

2 NUMERICAL METHOD

The code used is an incompressible finite volume Navier-Stokes solver called CALC-BFC [7]. The solver is based on structured grids and the use of curvi-linear boundary fitted coordinates. The grid arrangement is collocated and the Rhie and Chow interpolation method [8] is used. The code is parallelised for 3D flows [9] using block decomposition and the message passing systems PVM and MPI. For the advancement in time, the Crank-Nicolson scheme is used and the momentum equations are discretized in space using 2nd order difference schemes (the central difference scheme (CDS) and the van Leer scheme). The PISO algorithm [10] is used for the pressure-velocity coupling. As a subgrid scale model, the Smagorinsky model is used with the Smagorinsky constant equal to 0.1.

3 BOUNDARY CONDITIONS

In the computations on the *UMIST mesh* (see Fig. 4), no-slip condition is applied at the airfoil wall. In the computations on the *Chalmers mesh* (see Fig. 6), the no-slip condition is compared to an approximate wall boundary condition, based on the instantaneous log-law. The inlet is specified all over the curved areas of the C-meshes. The velocities are set to $\overline{u} = \cos \alpha U_\infty$ and $\overline{v} = \sin \alpha U_\infty$, where U_∞ is the freestream velocity. At the outlet, a convective boundary condition is applied: $\frac{\partial \phi}{\partial t} + U_\infty \frac{\partial \phi}{\partial x} = 0$. A Neumann boundary condition is used for the pressure at all boundaries ($\frac{\partial \overline{p}}{\partial n} = 0$) and periodic boundary conditions are used in the spanwise direction.

4 DISCRETIZATION SCHEMES OF THE CONVECTIVE TERMS

When the momentum equations are discretized in space using the central difference scheme (CDS), considerable unphysical oscillations are present all over the computational domain (see Fig. 2). The CDS is often used in LES because of its non-dissipative and energy-conserving properties. However, the scheme is also known to produce these odd-even oscillations (grid-to-grid oscillations or wiggles) when the resolution is poor.

To remove the unphysical oscillations in front of the airfoil and upstream of the transi-

tion region, a bounded second-order upwind discretization scheme (the van Leer scheme) is used in this region. The schemes are blended in the transition region, so that the convective flux can be expressed as:

$$\dot{m}u_{UDS}^m + \dot{m}\left[\alpha u_{CDS}^{m-1} - \alpha u_{UDS}^{m-1} + (1-\alpha)u_{UDScorr}^{m-1}\right] \ , \tag{1}$$

where CDS stands for the central difference scheme, UDS for the 1st-order upwind scheme and $UDScorr$ for the 2nd-order correction to the lower order upwind scheme ($m-1$ is the previous iteration). Here α is a blending function ($0 \le \alpha \le 1$) and, at the extremes, we have:

$\alpha = 0$:   the van Leer scheme
$\alpha = 1$:   the central difference scheme with deferred correction

The blending function used in the computation on the UMIST mesh blends the two schemes from 1 to 8 % of the chord on the suction side and from 4 to 19 % on the pressure side.

Upwinding removes unphysical oscillations, not only in the part of the domain where upwinding is used but also downstream of the area where the mixing between the two schemes is applied. This can be seen in Fig. 3, where the resolved stresses in the wall-normal direction are shown. Note that not all unphysical oscillations are abscent in the CDS-region (mainly because of the coarse resolution in the streamwise direction). These result in high values of the resolved stresses, in the outer parts of the boundary layer (see Fig. 3).
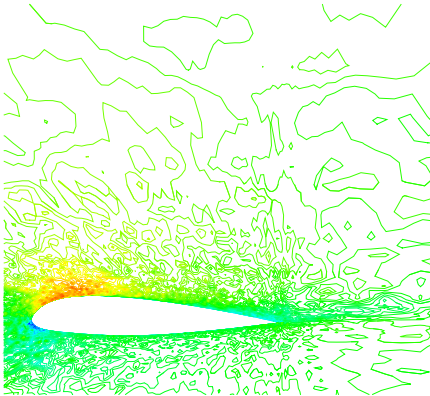

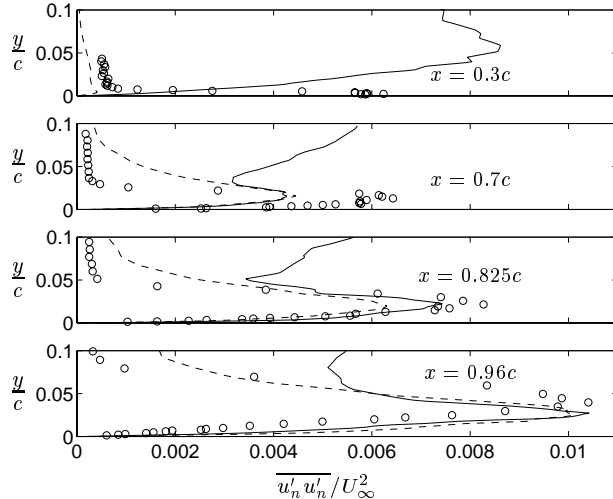Figure 2: Instantaneous $\overline{u}$-velocity when central differencing is used on the UMIST mesh (Comp. # 1).

Figure 3: Spanwise and time averaged resolved $\overline{u_n' u_n'}$-velocity fluctuations. Solid: Comp. # 1 (CDS); dashed: Comp. # 2 (upwinding); circles: exp. (F2).
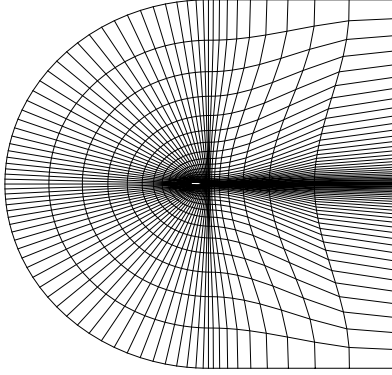
4

Figure 4: The UMIST mesh: $321 \times 65 \times 33$ nodes (every 4th node in the i-direction and every 2nd node in the j-direction are plotted).
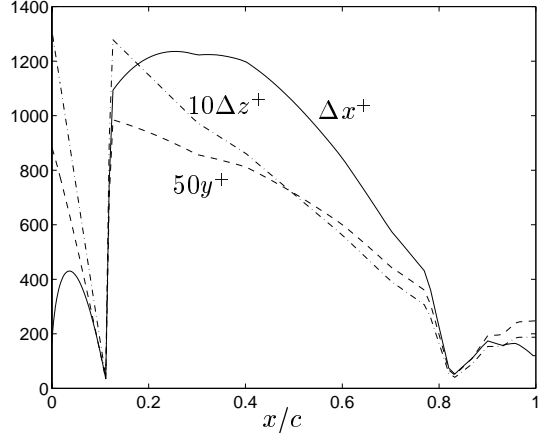

Figure 5: The size of the cell and the distance to the nearest node in dimensionless wall units along the suction side of the airfoil wall on the UMIST mesh ($L_z = 0.03c$).

5   MESHES

Although the unphysical oscillations are suppressed and dampened upstream respectively downstream of the transition region, the present grid, the UMIST mesh (see Fig. 4), is far too coarse to be able to do a useful LES. The mesh consists of $321 \times 65 \times 33$ grid-nodes; the resolution on the suction side of the airfoil is shown in Fig. 5. In order to be able to do a useful LES when wall functions are used, the size of the cells in the streamwise direction near the wall should be less than 600 wall units [11]. Judging from this limit, the resolution is very poor. Δx^+ exceeds 1200 and the maximum is in the transition region. Besides, the no-slip condition is used.

A new mesh was constructed (see Fig. 6) that consists of $720 \times 65 \times 33$ nodes, more than twice as many nodes in the i-direction (the wrap-around-direction in the C-mesh). Fig. 7 shows the wall resolution on the suction side of the airfoil on the new mesh. Here, Δx^+ does not exceed 600. Δx is increased linearly from the leading edge to the trailing edge on the suction side and the stretching is very low (which is crucial for the energy conservation, see e.g. [12]) Overall, the stretching in this direction is less than 5.9% (the maximum is in the wake near the trailing edge). Besides the resolution in the i-direction, this is one of the main differences as compared with the former mesh, in which the maximum stretching is 29.2% (just downstream of the trailing edge). Other differences are that the new mesh is refined along the wake and that the resolution in the wall-normal direction near the trailing edge and in the wake is much coarser on the new mesh, which can be a problem in the wake where the mixed shear layer should be sufficiently resolved.
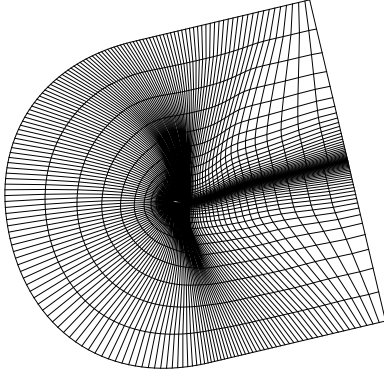
5

Figure 6: The Chalmers mesh: $720 \times 65 \times 33$ nodes (every 4th node in the i-direction and every 2nd node in the j-direction are plotted).
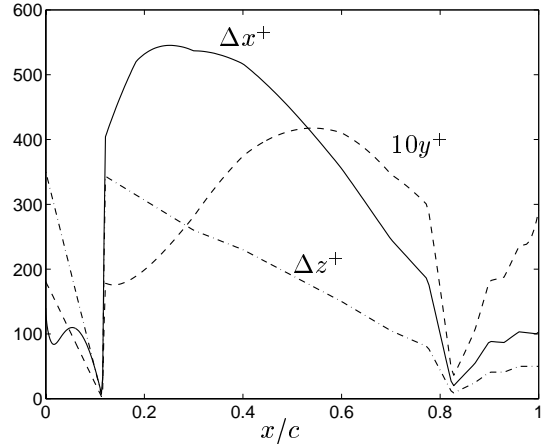

Figure 7: The size of the cell and the distance to the nearest node in dimensionless wall units along the suction side of the airfoil wall on the Chalmers mesh ($L_z = 0.08c$).

5.1 The resolution and extension in the spanwise direction

The extent in the spanwise direction for the airfoil case was initially chosen as $L_z = 0.03c$. Near the trailing edge, however, the boundary layer thickness, δ_{99}, from the experiments, is about 9 % of the chord, three times larger than L_z. When periodic boundary conditions are used, these conditions imply that the extent in the spanwise direction should be wider than the largest structures in that direction. The largest scales in a boundary layer are in the order δ_{99} and these scales are probably also apparent in the spanwise direction; thus the ratio δ_{99}/L_z should at least be less than one. L_z was set to $0.08c$ on the Chalmers mesh. Thirty-two cells are used in the spanwise direction for both meshes, resulting in almost three times coarser resolution compared to the UMIST mesh and Δz^+_{max} is approximately 350 on the Chalmers mesh (in Figs. 5 and 7 the wall units $\left(\frac{u_\tau}{\nu} \right)$ are computed from the skin friction coefficient from the experimental data, the y^+ and Δz^+ from the predicted friction velocity are shown in Figs. 16 and 18).

6 APPROXIMATE WALL BOUNDARY CONDITIONS

In a wall-resolved LES, the distance from the wall to the first node should be at least less than two wall units $\left(\frac{u_\tau}{\nu} \right)$. Although the velocity profile in the viscous sublayer ($y^+ < 5 - 8$) is linear in the mean, instantaneously this need not be the case and y^+ must be less than two in order to resolve the velocity gradient close to the wall. In addition however, in a wall-resolved LES, the structures close to the wall, especially the important energy-producing structures, need to be sufficiently resolved. There are streamwise counter-rotating vortices in the viscous sublayer, the *streaks*. These structures have an approximate spanwise periodicy of 100 wall units and a length of 1000 wall units.

It is important to capture these near-wall streaks as they interact with the buffer region and are responsible for a major part of the energy production in this region through the *bursting* process [13]. Other mechanisms in the buffer region are *sweeps* (when high-speed fluid from the logarithmic region enters the buffer region) and *ejections* (when low-speed fluid from the buffer region enters the logarithmic region). All these coherent structures can be captured in a wall-resolved LES if the sizes of the cells closest to the wall are within the range of $50 < \Delta x^+ < 150$, $\Delta y^+ < 4$ and $15 < \Delta z^+ < 40$ [11].

A wall-resolved LES of the near-wall streaks in the turbulent boundary layer on the airfoil is not feasible owing to the required computer power. At this high Reynolds number ($Re_c = 2.1 \cdot 10^6$), the near-wall problem of LES is evident. The use of approximate wall boundary conditions are necessary. Grids with a lot coarser resolution in the spanwise and streamwise directions are then used and the first node from the wall is placed in (the buffer region or) the logarithmic region. With such a grid, many of the coherent structures will not be sufficiently resolved and the sublayer streaks are not resolved at all.

Numerically, when the near-wall resolution is insufficient, the correct value of the wall shear stress ($\tau_{wall} = \nu \left(\partial \overline{u}/\partial y \right)_{wall}$) needs to be determined. The wall shear stress is usually assumed to be correlated to the velocity in the log region through the use of a near-wall law, e.g. the power law or the log law. In the present work the instantaneous log law is used in the log region ($y^+ \geq 30$):

$$\bar{u}^+ = \frac{\ln y^+}{\kappa} + B \ , \tag{2}$$

where $\kappa = 0.4$, $B = 5.2$.

The wall-normal cell size (Δy) at the leading and trailing edge must be very small in order to sufficiently resolve the very thin laminar boundary layer and the mixed shear layer. When generating meshes, this will result in the cells having small Δy in the wall-bounded turbulent boundary layers as well. For that reason, the y^+ may often be located in the buffer region ($5 \leq y^+ \leq 30$) in which the following wall law is used:

$$\bar{u}^+ = \frac{\ln y^+}{C} + D \ . \tag{3}$$

Eq. 3 is a matching between the log law (Eq. 2) and the linear law in the viscous sublayer ($y^+ \leq 5$):

$$\bar{u}^+ = y^+ \ . \tag{4}$$

The constants in Eq. 3 becomes $C = \ln 6 / (\frac{1}{\kappa} \ln 30 + B - 5)$ and $D = 5 - C \ln 5$.

These wall functions (Eqs. 2-4) are compared to the no-slip condition in the computations on the Chalmers mesh. The relation between the cells compared to the 'ideal' size is visualised in Fig. 8 at three different streamwise locations, just after the transition, before the separation and in the separation region. The 'ideal' size refers to a resolution
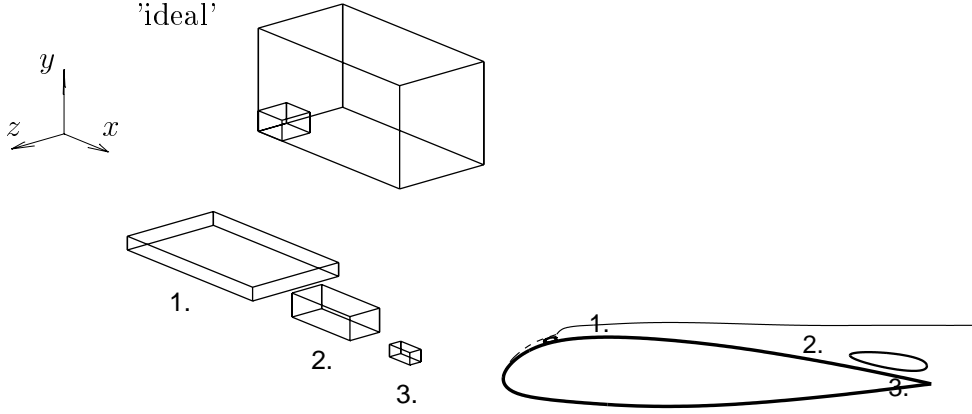
Figure 8: The size of the cells in dimensionless wall units on the Chalmers mesh compared with the 'ideal' size when wall functions are used (the smaller box = $[100, 60, 100] < [\Delta x^+, \Delta y^+, \Delta z^+] < [600, 300, 300]$ = the larger box): 1. just after the transition, 2. before the separation, 3. in the separation region ($L_z = 0.08$, 32 cells in the spanwise direction).

of $[100, 60, 100] < [\Delta x^+, \Delta y^+, \Delta z^+] < [600, 300, 300]$ [11]. In addition, the ratio between Δz^+ and Δy^+ should preferably be in the order of one [14]. This is not the case just after the transition as can be seen in Fig. 8, where $\left(\frac{\Delta z^+}{\Delta y^+}\right)_{max} \approx 10$.

The approximate wall boundary condition is implemented in the code by adding a viscosity, $\nu_{B.C.}$, to the laminar viscosity on the wall. The friction velocity, u_τ (and τ_{wall}), is determined from Eqs.2-4. From the relation

$$\frac{\tau_{wall}}{\rho} = u_\tau^2 = \nu \frac{\partial \bar{u}}{\partial y}\bigg|_{wall} = \left(\nu + \nu_{B.C.}\right)\frac{\bar{u}_P}{y_P} \ , \tag{5}$$

the viscosity on the wall could be expressed as

$$\nu + \nu_{B.C.} = \frac{u_\tau y_P}{\bar{u}_P^+} \ . \tag{6}$$

Note that the numerical boundary condition for $\bar{u}$, $\bar{v}$ and $\bar{w}$ at the wall is no-slip according to Eq. 5. The product of the artificial viscosity at the wall, $\nu + \nu_{B.C.}$, and the linear velocity assumption between the near-wall node and the wall (see Eq. 5) give the wall shear stress τ_{wall} according to the wall functions.

7 EFFICIENCY OF THE PARALLELIZATION

For the present flow, the required number of nodes in order to do a LES is in the order of millions. This is true, even though the transition is prescribed and the effects of the very near-wall structures are modeled by approximate boundary conditions. It is

also estimated that about $10 - 20$ time units (1 time unit $= c/U_\infty$, where c is the airfoil chord and U_∞ is the freestream velocity) of simulation are required to be able to gather reliable statistics; with a time step of $3 \cdot 10^{-4} c/U_\infty$ (the present time step), the number of time steps would be at least 33000. The need for an efficient numerical method and effective parallelization is obvious. The present code is parallelized for 3D flows [9] using block decomposition and PVM and MPI as message passing systems. The code has been ported to a SUN Enterprise 10000 at Chalmers and the IBM SP at the Center for Parallel Computing at KTH.

7.1 Convergence criteria

For the velocities, the convergence criteria is that the L^1-norm of the residuals of the discretized momentum equations scaled with $\rho U_\infty A_{inlet} U_\infty$ should be less than the desired convergence level, η, where A_{inlet} is the projected area of the inlet. Here, the criteria is checked immediately after the solver (but of course without under-relaxation), i.e. the residuals are calculated with the 'old' coefficients and before the correction in the PISO algorithm. For the continuity equation, the criterion is that the L^1-norm of discretized finite-volume continuity error scaled with the inlet mass flow should be less than η.

In the computations on the UMIST mesh, the convergence level is set to $1 \cdot 10^{-3}$ and with a time step of $3 \cdot 10^{-4} c/U_\infty$, there are three global iterations per time step for Comp. # 1 which decreases to two iterations for Comp. # 2 (the one with upwinding scheme, see Table 2). In these two computations, the convergence criteria for the continuity equation is well fulfilled (it is fulfilled immediately at each time step). The scaled L^1-norm is approximately $1 \cdot 10^{-4}$. It is noteable that the convergence within each time step is very slow. The PISO algorithm [10] is used for the pressure-velocity coupling, with two additional corrector steps beside the first SIMPLE step. The algorithm was found to be more efficient than the optimised SIMPLEC algorithm in a previous study on a backward-facing step flow [15]. In the present airfoil case, it is the convergence of the pressure-correction equation that sets the limit on the convergence rate, at least for the computations on the finer mesh (the Chalmers mesh). Here, the scaled L^1-norm is approximately $1 \cdot 10^{-3}$ and sometimes exceeds the convergence level, η. Because of the very slow convergence within each time step, the approach of simply limiting the number of global iterations per time step is applied. For the computations on the Chalmers mesh, the number of iterations is set to two, corresponding to an η of approximately $1 \cdot 10^{-3}$.

7.2 Speed-up results

The elapsed time per time step is shown in Table 1 with the convergence criteria fulfilled after two global iterations ($\eta \approx 1 \cdot 10^{-3}$). The computational domain is decomposed into eight, 16 and 32 subdomains. No significant decrease in the convergence rate is observed when 16 and 32 subdomains are used. Two different versions of the message passing PVM are available on the SUN computer: a shared memory based PVM and a socket based

Mesh	Computer & message passing system	Number of processors		
		8	16	32
UMIST	SUN, PVM, socket based	$48s$	$38s$	$36s$
	SUN, PVM, shared memory based	$24s$	$(12s)$	$(6s)$
	SUN, MPI	$24s$	-	-
	IBM SP, PVM	$12s$	-	-
	IBM SP, MPI	-	$5.4s$	$2.8s$
Chalmers	IBM SP, MPI	-	-	$6.0s$

Table 1: Elapsed time per timestep on the UMIST and Chalmers meshes (722568 and 1617924 computational nodes, respectively).

PVM. When eight processors are used for the present case, the shared memory based PVM is twice as fast as the socket based PVM. The simulation of one time unit requires about 180 CPU hours and the solution is advanced in time by about one time unit per day.

The IBM SP computer is faster. The simulation of one time unit requires about 83 CPU hours and with MPI and 32 processors the solution is advanced 9 time units per day. On this computer, an approximately linear speed-up is obtained between the eight and 32 processor cases. On the finer mesh, the elapsed time per time step is $6s$ and the simulation of one time unit requires about 180 CPU hours. The solution is advanced more than four time units per day, which is quite acceptable for industrial use.

8 RESULTS

Four computations are presented in this paper. The set-up differences are summarised in Table 2. The averaging times are at least six time units, which is checked to be reasonably sufficient, even for second-order statistics, when the boundary layer remains attached. The initial conditions are 2D $k - \varepsilon$ solutions for Comp. # 1 and # 3 and the previous LES for Comp. # 2 and # 4. The time step is $3 \cdot 10^{-4} c/U_\infty$ for all computations, giving a maximum CFL number of 1.3 for Comp. # 1. When upwinding is used on the UMIST mesh it decreases a great deal ($CFL_{max} \approx 0.6$). For the computations on the finer mesh, the maximum CFL number is approximately 1.
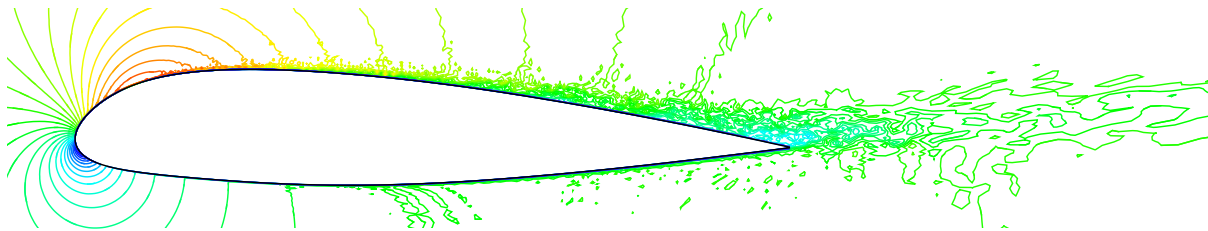

Figure 9: Instantaneous $\bar{u}$-velocity on the Chalmers mesh when wall functions are used (Comp. # 4).
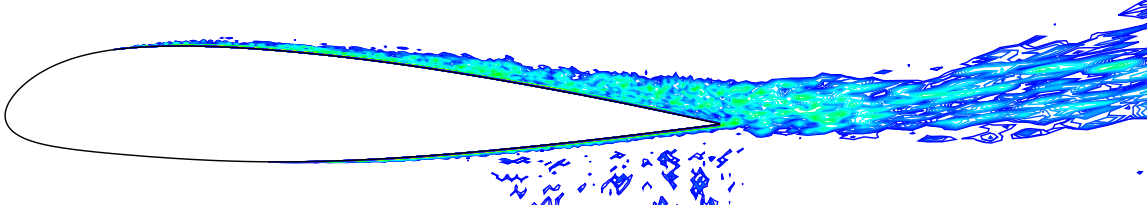
10

Figure 10: Instantaneous Smagorinsky eddy viscosity on the Chalmers mesh when wall functions are used (Comp. # 4). The contour levels are logarithmic.

Computation	# 1	# 2	# 3	# 4
Mesh	UMIST $321 \times 65 \times 33$		Chalmers $720 \times 65 \times 33$	
Spanwise ext.	$L_z = 0.03c$		$L_z = 0.08c$	
Convective scheme	CDS	van Leer $(x/c < 0.01)$ + CDS $(x/c > 0.09)$	van Leer $(x/c < 0.02)$ + CDS $(x/c > 0.12)$	
SGS model	Smagorinsky		no model $(x/c < 0.12)$ + Smagorinsky $(x/c > 0.23)$	
Wall b. c.	$\longleftarrow$ no-slip $\longrightarrow$			Eqs. 2-4

Table 2: Computational parameters that differ for the four computations. The Smagorinsky constant is set to 0.1.

In the computations on the Chalmers mesh, the extent of the mixing region between the two schemes were moved slightly downstream in order to more accurately prescribe the transition at the location given in the experiments (at 12% of the airfoil chord). The CDS is fully active just downstream of that point and is gradually mixed with the van Leer scheme, which is fully active upstream of location $x = 0.02c$. In the Smagorinsky model, the eddy viscosity is not zero in the laminar region (the strain is not zero). To prescribe the transition in a more accurate way, the Smagorinsky eddy viscosity is set to zero upstream of the transition point and is gradually mixed with the eddy viscosity downstream of that point. At 23% of the airfoil chord, the Smagorinsky model is fully active. A similar approach is applied around the transition point on the pressure side of the airfoil.

The transition and growth of the turbulent boundary layer is clearly visiualized in the computations on the finer mesh, when looking at instantaneous contourplots of the resolved velocity and the Smagorinsky eddy viscosity (see Figs. 9 and 10). The very thin turbulent boundary layer on the pressure side is also visible in the figures, as well as some unphysical oscillations outside of the thin layer, owing to a coarser resolution in the

Figure 11: Instantaneous resolved pressure on the Chalmers mesh when wall functions are used (Comp. # 4).

streamwise direction on this side. A contour plot of the instantaneous resolved pressure is shown in Fig. 11.

Although the resolution is increased in the streamwise direction and approximate wall boundary conditions are applied, the pressure peak at the leading edge is underpredicted and we fail to predict the plateau, the decrease in the adverse pressure gradient, that should be present in the separation region (see C_p in Fig. 12). Consequently none of the present computations predict the separation near the trailing edge (a small separation bubble is occasionally instantaneously formed) and the skin friction coefficient remains positive (see Fig. 12).
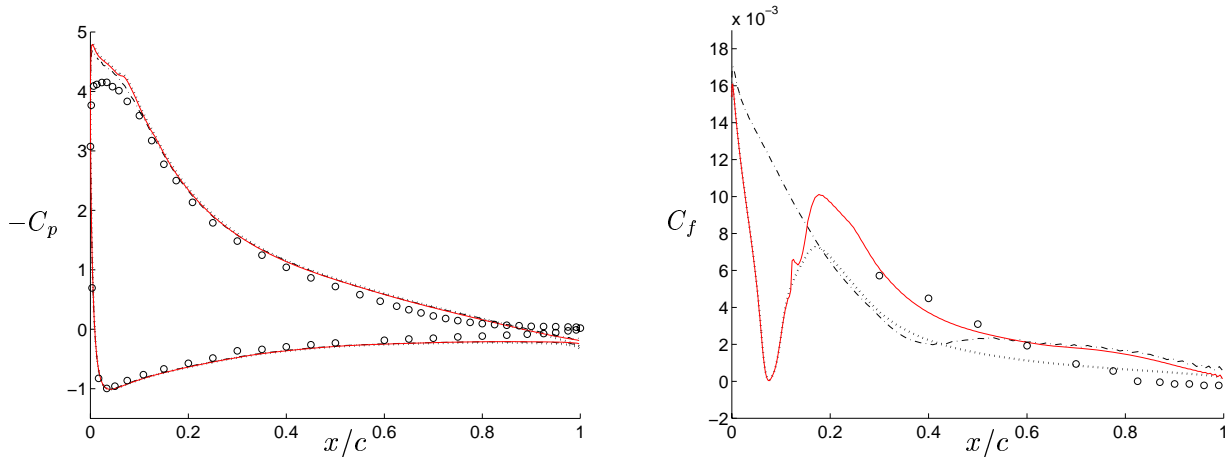
Figure 12: The pressure coefficient (left figure) and the skin friction coefficient (right figure). Red solid: approximate wall boundary condition, Eqs. 2-4 (Comp. # 4); dotted: no-slip wall boundary condition (Comp. # 3); dash-dotted: Comp. # 2; circles: exp. (F2).

8.1 Effect of the approximate wall boundary condition

Comparing Comp. # 4 and # 3, the use of the approximate wall boundary condition (Eqs. 2-4) has a significant effect on the results (see e.g. Fig. 20). Looking at the artificial viscosity at the wall (Fig. 13), this is not great compared with the values at the near-wall node (Fig.14), but it works to decrease the eddy viscosity at the near-wall node, which
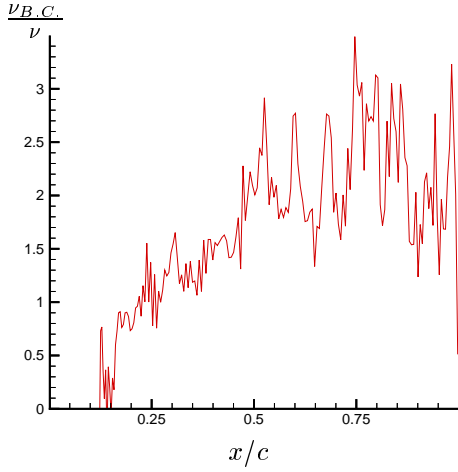
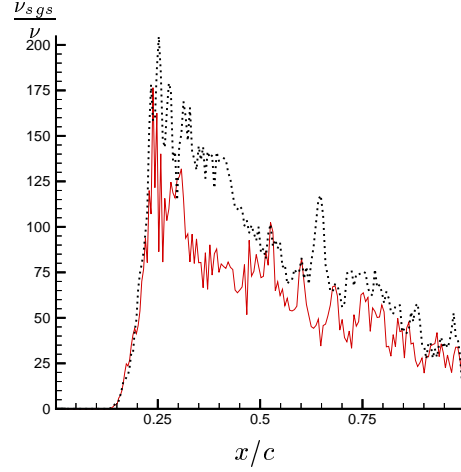Figure 13: Instantaneous viscosity $\nu_{B.C.}$ on the wall, see Eq. 6 (Comp. # 4).

Figure 14: Instantaneous Smagorinsky eddy viscosity at the near-wall node. Red solid: approximate wall boundary condition, Eqs. 2-4 (Comp. # 4); dotted: no-slip wall boundary condition (Comp. # 3).
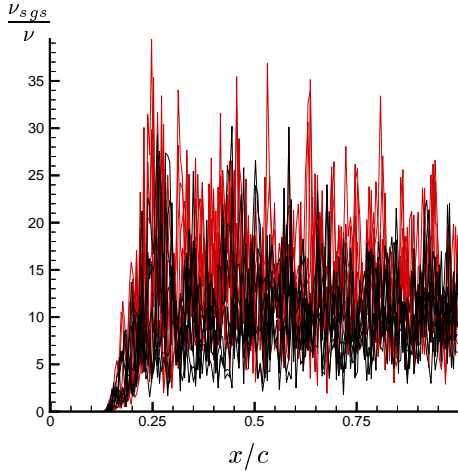

Figure 15: Instantaneous Smagorinsky eddy viscosity at nodes 2 to 9 from the wall. Red: approximate wall boundary condition, Eqs. 2-4 (Comp. # 4); black: no-slip wall boundary condition (Comp. # 3).
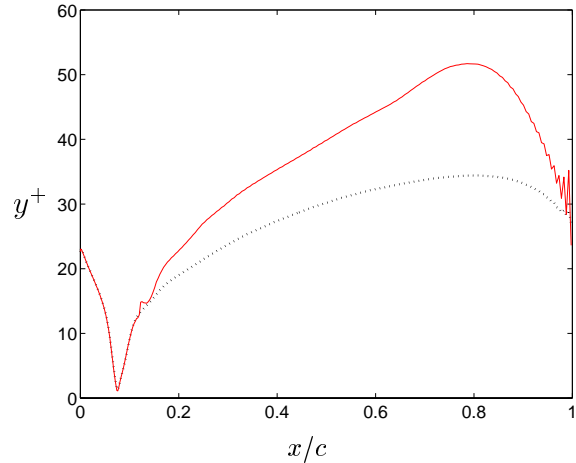

Figure 16: Spanwise and time averaged wall distance (in dimensionless wall units $y^+ = y u_\tau / \nu$) at the near-wall node based on the predicted friction velocity. Red solid: approximate wall boundary condition, Eqs. 2-4 (Comp. # 4); dotted: no-slip wall boundary condition (Comp. # 3).

is located in the lower parts of the logarithmic region (see Fig. 16). The eddy viscosity is increased further away from the wall as compared with when the no-slip condition is used (see Fig. 15).
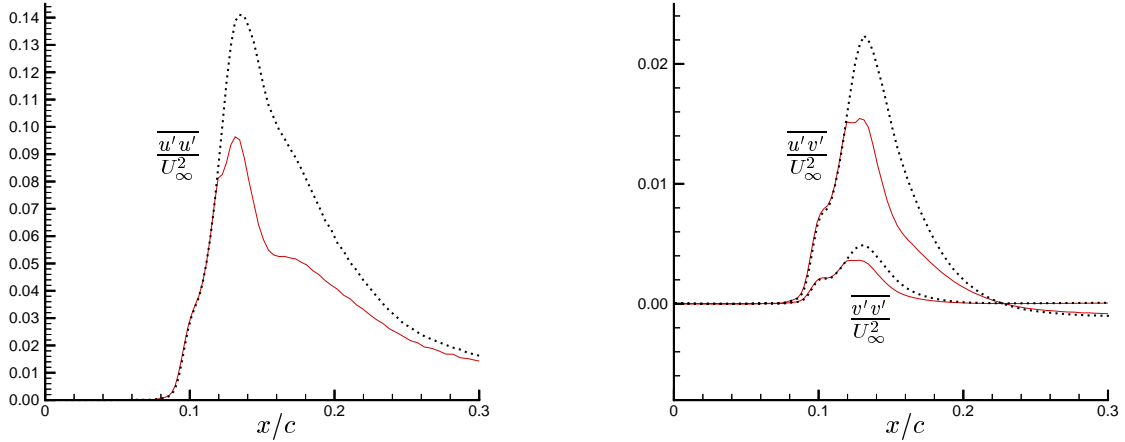
Figure 17: Spanwise and time averaged resolved velocity fluctuations at the near-wall node in the transition region. Red solid: approximate wall boundary condition, Eqs. 2-4 (Comp. # 4); dotted: no-slip wall boundary condition (Comp. # 3).

8.2 Transition

When α is larger than approximately 0.6 in the mixed scheme (see Eq. 1 and Table 2), the non-dissipative effects of the CDS give rise to numerical oscillations and the boundary layer is tripped numerically. The resolved stresses at the near-wall node (shown in Fig. 17) are very high, especially in the x-direction. Unfortunately, no experimental data are available in the transition region, but for Comp. # 3, the $\overline{u'u'}$-peak is almost five times larger than the maximum stresses from the experiments near the trailing edge. The Smagorinsky eddy viscosity at the same near-wall nodes (Fig 14), in the beginning of the mixed region (e.g. at $x = 0.15c$), is very low. The CDS is fully active already at 12% of the chord, suggesting that the maximum peaks in the stresses (at about 13% of the chord) are unphysical and due to the central difference scheme alone. The unresolved stresses should most likely account for a significant part of the stresses (using these coarse grids in the transition region) and the transition could be prescribed more accurately by letting the Smagorinsky model damp the resolved stresses in the transition region.

The approximate wall boundary condition has an dampening effect on the resolved stresses, in the transition region and a bit downstream (from 12 to approximately 30 percent of the chord, see Fig. 17). Further downstream (see Fig. 20), the wall functions increase the magnitude of the stresses and they are closer to the experimental results.

8.3 Resolution in the streamwise and spanwise direction

The effect of the increased streamwise resolution is for instance seen in the outer parts of the boundary layer (see Fig. 20). Not only the resolved stresses, but also the eddy viscosity, goes down to zero in the outer parts. This is seen in the sharp boundary
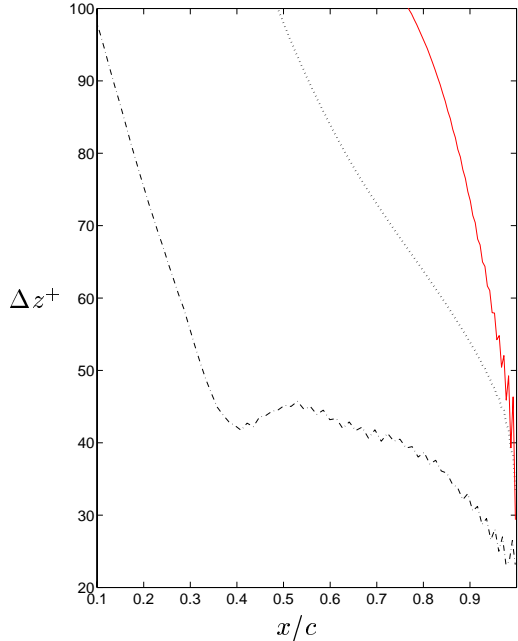
14

Figure 18: Spanwise and time averaged resolution in the spanwise direction based on the predicted friction velocity (in dimensionless wall units $\Delta z^+ = \Delta z u_\tau/\nu$). Red solid: Comp. # 4; dotted: Comp. # 3; dash-dotted: Comp. # 2
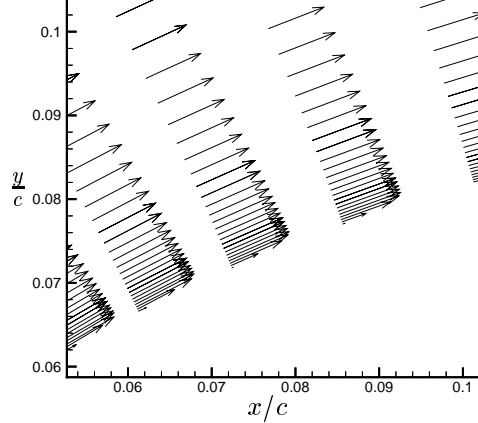
Figure 19: Vector plot of the laminar boundary layer at the leading edge showing incipient separation (every 7th vector in the streamwise direction is shown).

layer edges in the velocity profiles. The major difference between Comp. # 2 and the computations on the Chalmers mesh is seen in the skin friction coefficient, where Comp. # 2 completely fails to capture the laminar separation bubble, contrary to Comp. # 3 and # 4, where there is a clear indication of the laminar separation bubble at about 7% of the chord (see Fig. 12). Also note the little plateau in the pressure coefficient, indicating separation.

Although incorrectly predicted, the effect of the small spanwise extent need not be that significant, in these attached boundary layer computations. The maximum boundary layer thickness near the trailing edge is about $4-5\%$ of the chord and $L_z = 0.03c$ may be enough to resolve the largest structures in that direction (see Sec. 5.1).

It is noteable that we get worst results for Comp. # 3 and very similar results for computation # 2 and # 4 around the rear part of the airfoil ($x/c > 0.5$). This is true for the velocity profiles as well as the magnitude of the shear stresses (see Fig. 20). This might be an effect of the spanwise resolution. As seen in Fig. 18, the *computed* spanwise resolution (based on the predicted friction velocity) for Comp. # 2 is less than 45 wall units at the rear 65% of the profile. It is likely that the near-wall streaks is starting to be resolved, thanks to the spanwise resolution. This is also noted as an increase in the skin friction coefficient (see Fig 12). This increase in C_f is not seen for Comp. # 3 (where the computed Δz^+ never gets fine enough to resolve the near wall streaks (see Fig. 18))
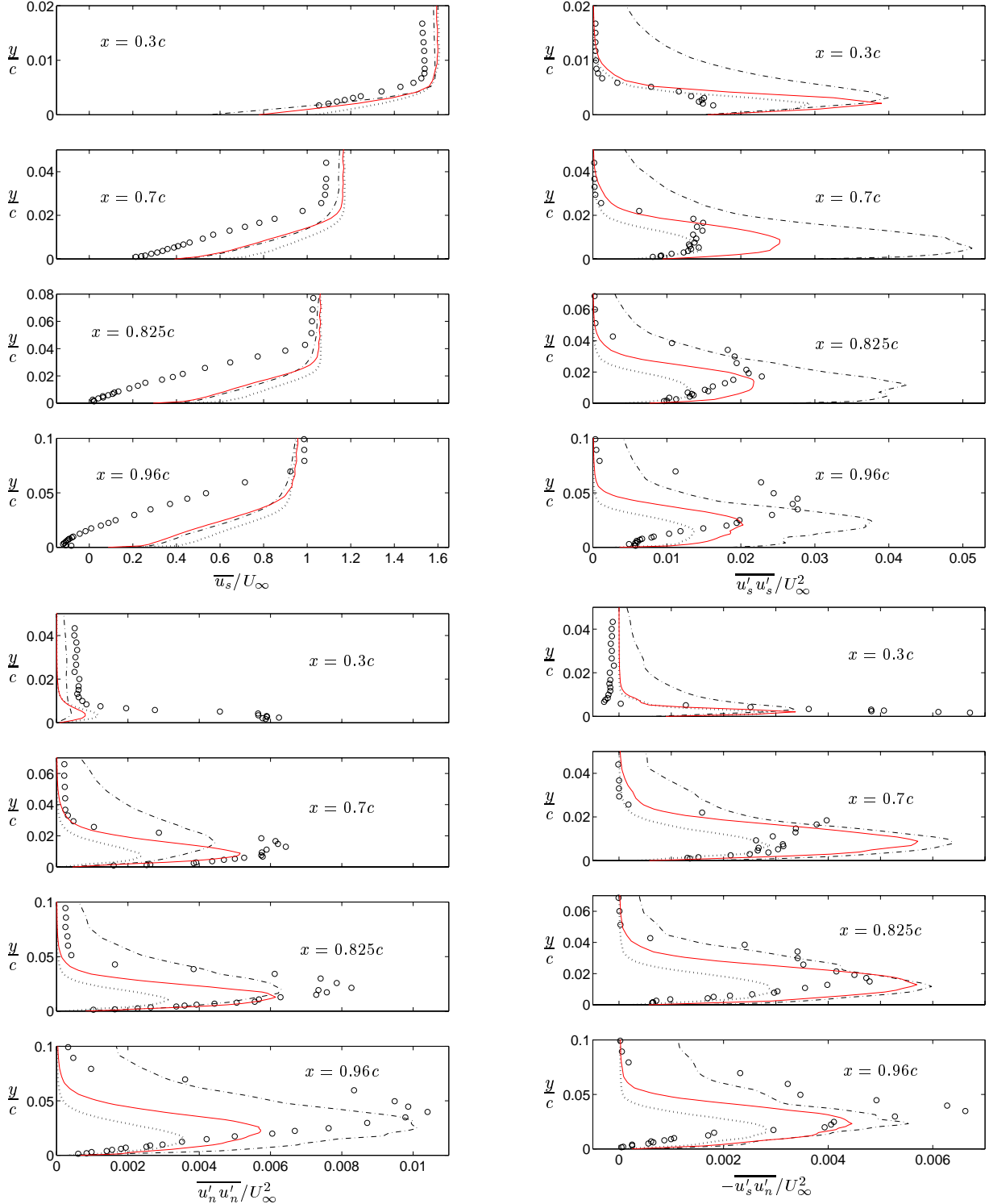
15

Figure 20: Spanwise and time averaged first- and second-order statistics. Red solid: approximate wall boundary condition, Eqs. 2-4 (Comp. # 4); dotted: no-slip wall boundary condition (Comp. # 3); dash-dotted: upwinding scheme on the UMIST mesh (Comp. # 2); circles: exp. (F2). Subscripts s and n denote the directions parallel and normal to the airfoil wall, respectively.

and not for Comp. # 4 either, but the approximate wall boundary condition seems to take these effects into account, right from where the transition starts. The spanwise resolution seems to be very important, in that Comp. # 3 with a finer resolution in the streamwise direction, produces worse results than Comp. # 2. It is encouraging that the wall functions seem to have their intended effect and handle the coarse spanwise resolution.

8.4 Lift and drag coefficients

Table 3 shows the lift and drag coefficients for the different computations. The lift coefficients from the computations are overpredicted. They increase somewhat when upwinding is used. The drag coefficients decrease significantly when upwinding is used and even more for Comp. # 3 and # 4. Comparing Comp. # 3 and # 4, there is a tendency toward the experimental results when the approximate boundary condition is used.

	Exp. F1	# 1	# 2	# 3	# 4
C_L	1.56	1.68	1.72	1.75	1.72
C_D	0.0204	0.0374	0.0280	0.0167	0.0170

Table 3: Spanwise and time averaged lift and drag coefficients for the four computations and the experiment in the F1 wind-tunnel.

Figs. 21-23 show the time history of the lift and drag coefficients. It is interesting to note that the drag coefficient varies between approximately 0.013 and more than twice that (0.0275). Fig. 24 shows the frequency spectrum of the lift coefficient. Although the magnitude of the oscillations vary a lot, there is a distinct peak in the frequency spectrum at a Strouhal number of 8.6.
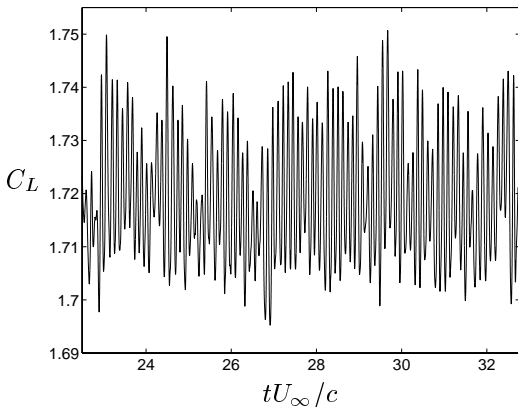

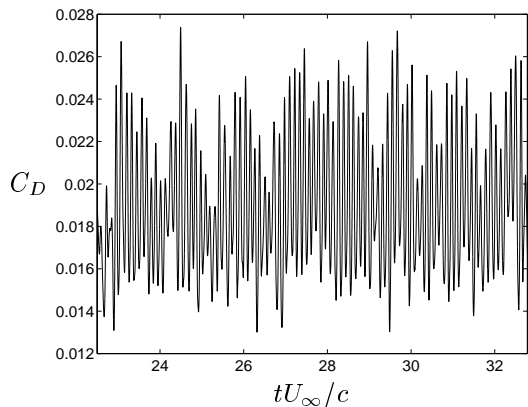Figure 21: Time history of the lift coefficient for Comp. # 4.

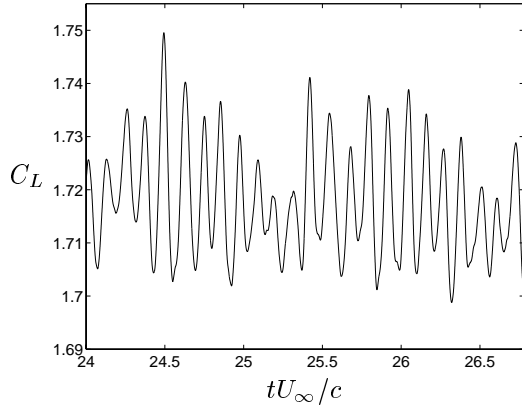Figure 22: Time history of the drag coefficient for Comp. # 4.

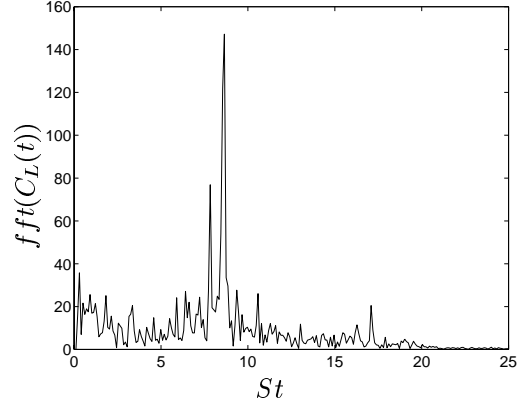Figure 23: Time history of the lift coefficient for Comp. # 4.

Figure 24: Frequency spectrum of the C_L signal for Comp. # 4.

9 CONCLUSIONS AND FUTURE WORK

Although none of the present computations predict separation, it is encouraging that the wall functions seem to take into account the low resolution in the spanwise direction (in these attached boundary layer simulations) and hope is that this is true in the other directions as well.

The transition process and the behaviour of the SGS-model and CDS in that region also need further examination to prescribe the transition in a more natural way.

However, one of the major problems seem to be in the laminar region and the resolution of the laminar boundary layer. It is in this region, around the leading edge, where the favorable pressure gradient accelerates the flow. This accelerated flow, certainly affects the region downstream and has an impact on the separation near the trailing edge. It is evident from the results (C_f, the underpredicted pressure at the leading edge and the overpredicted boundary layer edge velocity (at e.g. $x = 0.3c$)) that the simulations have failed at the leading edge. In the computations, at the location where the boundary layer is as thickest, there are about 4-5 nodes in the wall-normal direction (see Fig. 19). And at the very leading edge ($x/c < 0.01$) there is only one node in the boundary layer. The resolution must probably be finer in this direction, making the prediction of the flow in this region more accurate. Alternatively, some approach (e.g. wall functions) must be applied in this region.

Furthermore, the separation region near the trailing edge is fairly thin and the use of a y^+ requirement for wall functions does not make any sense here. The separation region needs to be sufficiently resolved, not in a DNS-sense, but in the sense that a sufficient number of cells are used close to the wall to resolve the maximum backflow velocity [16]. In the Chalmers mesh, this region is captured with just 1-2 cells (in the wall-normal direction) downstream of the separation point, in the streamwise center of the separation bubble. This is inadequate and a modified mesh has been generated which will be used in the near future.

Acknowledgements

References

[1] L. Davidson. LESFOIL: an European project on large eddy simulations around a high-lift airfoil at high Reynolds number. In *ECCOMAS 2000, European Congress on Computational Methods in Applied Sciences and Engineering, 11-14 September*, Barcelona, Spain, 2000.

[2] EUROVAL- a European initiative on validation of CFD-codes. In W. Haase, F. Brandsma, E. Elsholz, M. Leschziner, and D. Schwamborn, editors, *Notes on Numerical Fluid Mechanics*, volume 42. Vieweg Verlag, 1993.

[3] ECARP- European Computational Aerodynamics Research Project: Validation of CFD Codes and Assessment of Turbulence Models. In W. Haase, E. Chaput, E. Elsholz, M. Leschziner, and U. Müller, editors, *Notes on Numerical Fluid Mechanics*, volume 58. Vieweg Verlag, 1997.

[4] L. Davidson and A. Rizzi. Navier-Stokes stall predictions using an algebraic stress model. *J. Spacecraft and Rockets*, 29:794–800, 1992.

[5] L. Davidson. Prediction of the flow around an airfoil using a Reynolds stress transport model. *ASME: Journal of Fluids Engineering*, 117:50–57, 1995.

[6] F.S. Lien and M.A. Leschziner. Modelling of 2D separation from high-lift aerofoils with a non-linear eddy-viscosity model and second-moment closure. *The Aeronautical Journal*, 99:125–144, 1995.

[7] L. Davidson and B. Farhanieh. CALC-BFC: A finite-volume code employing collocated variable arrangement and cartesian velocity components for computation of fluid flow and heat transfer in complex three-dimensional geometries. Rept. 92/4, Dept. of Thermo and Fluid Dynamics, Chalmers University of Technology, Gothenburg, 1992.

[8] C.M. Rhie and W.L. Chow. Numerical study of the turbulent flow past an airfoil with trailing edge separation. *AIAA Journal*, 21:1525–1532, 1983.

[9] H. Nilsson and L. Davidson. CALC-PVM: A parallel multiblock SIMPLE multiblock solver for turbulent flow in complex domains. Technical Report 98/12, Dept. of Thermo and Fluid Dynamics, Chalmers University of Technology, Gothenburg, 1998.

[10] R.I. Issa. Solution of Implicitly Discretised Fluid Flow Equations by Operator-Splitting. *J. Comp. Physics*, 62:40–65, 1986.

[11] U. Piomelli and J.R. Chasnov. Large-eddy simulations: Theory and applications. In D. Henningson, M. Hallbaeck, H. Alfreddson, and A. Johansson, editors, *Transition and Turbulence Modelling*, pages 269–336, Dordrecht, 1996. Kluwer Academic Publishers.

[12] T. Gough, S.Gao, P. Hancock, and P. R. Voke. Experiment and simulation of the tripped boundary layer on a flat plate: Comparative study. Technical Report ME-FD/95.40, Dept. of Mechanical Engineering, The University of Surrey, U.K., 1996.

[13] S.J. Kline, W.C. Reynolds, F.A. Schraub, and P.W. Runstadler. The structure of turbulent boundary layers. *Journal of Fluid Mechanics*, 30:741–773, 1967.

[14] C. Mellen. Private communication. Institut für Hydrodynamik, University of Karlsruhe, Germany, 1999.

[15] S. Dahlström and L. Davidson. Chalmers' 12-months report, task 4, LESFOIL: A Brite-Euram project. Technical report, Dept. of Thermo and Fluid Dynamics, Chalmers University of Technology, Gothenburg, Sweden, 1999.

[16] C. Mellen, J. Fröhlich, and W. Rodi. Karlsruhe's 24-months report, task 5, LESFOIL: A Brite-Euram project. Technical report, Institut für Hydrodynamik, University of Karlsruhe, Germany, 2000.